JTTEE5 11:320-332

Sealing Procedures for Thick Thermal Barrier Coatings

S. Ahmaniemi, J. Tuominen, P. Vuoristo, and T. Mäntylä

(Submitted 25 May 2001; in revised form 21 August 2001)

Zirconia-based $8Y_2O_3$-ZrO_2 and 22MgO-ZrO_2 thick thermal barrier coatings (TTBC, 1000 μm), were studied with different sealing methods for diesel engine applications. The aim of the sealing procedure was to improve hot corrosion resistance and mechanical properties of porous TBC coatings. The surface of TTBCs was sealed with three different methods: (1) impregnation with phosphate-based sealant, (2) surface melting by laser glazing, and (3) spraying of dense top coating with a detonation gun. The thicknesses of the densified top layers were 50-400 μm, depending on the sealing procedure. X-ray diffraction (XRD) analysis showed some minor phase changes and reaction products caused by phosphate-based sealing treatment and some crystal orientation changes and phase changes in laser-glazed coatings. The porosity of the outer layer of the sealed coating decreased in all cases, which led to increased microhardness values. The hot corrosion resistance of TTBCs against $60Na_2SO_4$-$40V_2O_5$ deposit was determined in isothermal exposure at 650 °C for 200 h. Corrosion products and phase changes were studied with XRD after the test. A short-term engine test was performed for the reference coatings ($8Y_2O_3$-ZrO_2 and 22MgO-ZrO_2) and for the phosphate-sealed coatings. Engine tests, duration of 3 h, were performed at the maximum load of the engine and were intended to evaluate the thermal cycling resistance of the sealed coatings. All of the coatings passed the engine test, but some vertical cracks were detected in the phosphate-sealed coatings.

Keywords diesel engine, hot corrosion, laser glazing, sealing, thermal barrier coating

1. Introduction

Plasma-sprayed zirconia coatings are widely used as thermal barrier coatings (TBCs) in gas turbine hot section components such as burners, transition ducts, and vanes. From the early 1980s, there have been many investigations to apply these coatings also in diesel engines.[1-4] The conditions in diesel engine combustion chambers differ considerably from those of gas turbine hot sections. Thermal and mechanical loads and hot corrosion conditions set very demanding requirements on thermal barrier coatings in both cases, but long-time durability of the coating is a more difficult problem in diesel engines. The major TBC failure mechanism that causes coating spallation in gas turbines is bond coat oxidation, whereas hot corrosion, thermal cycling, and mechanical loading are more expected coating failure modes in diesel engines. Low- and medium-speed diesel engines in marine and energy production applications use variable grades of fuels that may contain impurities such as S, V, and Na. In medium-speed production engines, the maximum combustion pressure and the mean temperature in the combustion chamber are considerably higher compared to high-speed diesel engines used in the automobile industry.

There have been several attempts to solve these problems by sealing the zirconia-based thermal barrier coating. Sealing of open porosity in TBC coating can be accomplished by liquid metal impregnation,[5] laser glazing,[6] hot isostatic pressing (HIP),[7] sol-gel processing, or by thin chemical vapor deposition (CVD) overcoatings.[8-11] Organic sealants are mainly used for corrosion protection at lower temperatures.[12] Yttria-stabilized zirconia, $8Y_2O_3$-ZrO_2, has been generally used in the gas turbine industry for years, but for diesel engine applications. Also, other stabilized zirconia structures have been considered. Namely, MgO, CeO_2, Sc_2O_3, In_2O_3, and Yb_2O_3 stabilized zirconia have been studied as more hot corrosion resistant coatings.[13] Other materials such as $ZrSiO_4$, Ca_2SiO_4, $CaTiO_3$, and $ZrTiO_4$ have been studied as hot corrosion resistant TBCs.[13] The thermal properties of these other coating materials are less favorable than are partially stabilized zirconia coatings because thermal conductivities are higher and coefficients of thermal expansion (CTE) are considerably lower. Mullite coatings have been studied to obtain better resistance against rapid thermal cycling.[3,14]

High expectations have arisen about the benefits of using TBCs in diesel engines. Some studies have shown that TBCs can increase the coefficient of thermal efficiency of diesel process and lower the fuel consumption.[15] Environmental aspects such as NO_x, SO_x, CO, CO_2, unburned hydrocarbons, and particle emissions have been studied in engine tests with and without TBCs.[1,3,15-18] Most of these studies disclose that TBCs decrease fuel consumption, but have a minor effect on emissions. In most cases, the NO_x emissions have increased because of higher combustion temperature, but the other emissions have decreased or remained unchanged. Without question the diesel process has to be adjusted correctly to utilize benefits of the thermal barrier coating. With TBCs the mean combustion temperature can be increased in the diesel process because of the insulating effect of the zirconia coating. At the same time the heat

S. Ahmaniemi, J. Tuominen, P. Vuoristo, and **T. Mäntylä,** Tampere University of Technology, Institute of Materials Science, P.O. Box 589, FIN 33101 Tampere, Finland. Contact e-mail: samppa.ahmaniemi@tut.fi.

Table 1 The Main Spray Parameters Used in the Air Plasma Spray (APS) Process

	Praxair ZRO 113/114, A/S	Praxair ZRO 103, F/C	AMDRY 962
Composition	$8Y_2O_3$-ZrO_2	22MgO-ZrO_2	Ni22Cr10A11Y
Particle size [μm]	−125 to +11	−75 to +10	−106 to +56
Argon flow rate [L/min]	35	35	55
Hydrogen flow rate [L/min]	12	2	9.5
Current [A]	600	600	600
Voltage [U]	71.0	70.3	70.5
Nozzle/electrode ∅ [mm]	6	6	6
Injector ∅ [mm]	1.8	1.8	1.8
Injector angle [°]	90	90	90
Axial powder feed distance [mm]	6	6	6
Spray distance [mm]	120	120	120
Powder feed rate [g/min]	48	28	75
Powder gas Ar flow rate [l/min]	2.6	2.4	4.1

losses to the cooling system decrease. This extra heat can be recovered in a turbocharger or in a flue gas boiler in a combined cycle.

This study examined thermal and mechanical properties of sealed TTBCs. The goal was to find methods to produce a dense top layer on a thick thermal barrier coating (TTBC) without losing the beneficial properties of the coating. Our earlier studies showed that an aluminum phosphate sealing treatment improved considerably the mechanical properties of thermally sprayed oxide coatings.[19-23] In this paper we compare three separate sealing methods and discuss their respective advantages and drawbacks.

Table 2 Abbreviations for the Studied Coating Systems

Coating System	Code
APS-sprayed $8Y_2O_3$-ZrO_2	8Y
APS-sprayed 22MgO-ZrO_2	22M
Laser-glazed $8Y_2O_3$-ZrO_2	8YL
Laser-glazed 22MgO-ZrO_2	22ML
Aluminum phosphate-sealed $8Y_2O_3$-ZrO_2	8Y AP
Orthophosphoric acid-sealed 22MgO-ZrO_2	22M OPA
8Y + D-Gun-sprayed $35SiO_2$-$65ZrO_2$	8Y $DZrSiO_4$
8Y + D-Gun-sprayed $8Y_2O_3$-ZrO_2	8Y D8Y
8Y + D-Gun-sprayed Cr_2O_3	8Y DC_2O_3

2. Experimental Procedure

2.1 Sample Preparation

Coatings of $8Y_2O_3$-ZrO_2 and 22MgO-ZrO_2 were air plasma sprayed (APS) with plasma spray equipment (Plasma-Technik A3000S, Sulzer Metco AG, Wohlen, Switzerland). Agglomerated and sintered (A/S) powder, ZRO 113/114 (Praxair, Indianapolis, IN), was the feedstock material for $8Y_2O_3$-ZrO_2 coatings and fused and crushed (F/C) ZRO 103 powder was the feedstock for the 22MgO-ZrO_2 coatings. Atomized AMDRY 962 MCrAlY powder was used as a bond coat material. The thickness of the bond coat was ~100 μm and top coat layers were ~1000 μm. The main spray parameters are presented in Table 1. Alloy 600 (74Ni16Cr8Fe1Mn0.5Cu0.5Si) was used as a substrate material for specimens in the hot corrosion test, whereas other coating specimens were prepared on AISI 4142 steel substrates. Substrates were buttons with height of 5 mm and diameter of 25 mm. All substrates were grit blasted just before spraying using 60 grit alumina and 4 bar air pressure. The back of the rotating specimen holder was air cooled during spraying. Abbreviations for all coating systems used in this study are presented in Table 2.

2.2 Laser Glazing

Coatings 8Y and 22M were laser glazed using a 4 kW continuous-wave, fiber-coupled model HL4006D lamp-pumped Nd:YAG laser (HAAS-Laser GmbH, Schramberg, Germany). In the glazing experiments the laser was equipped with an integrated water-cooled copper mirror with an effective focal length of 100 mm. The optimized continuous laser power in glazing processing was 3.5 kW and coating surface speed was 4500 mm/min. The width of the laser beam was 10 mm at the focused area, which was at a distance of 80 mm from the mirror. The specific energy density of the laser beam with the above-mentioned parameters is 4.7 J/mm^2. Two parallel 10 mm wide tracks, with 1 mm overlapping, were used to produce a 19 mm wide glazed zone. Before the final preparation of the studied coatings, laser-glazing parameters were optimized by comparing coating microstructures with different specific laser energy densities using continuous and pulsed laser beams. In the optimization stage of the laser glazing, the predetermined melting depth of the coating surface was reached, without causing coating spallation. In addition, introduction of vertical cracks, which pass through the thickness of the coating, was avoided.

2.3 Aluminum Phosphate Sealing Treatment

The 8Y coating was sealed with an $Al(OH)_3$-(85%) H_3PO_4 solution diluted with 20 wt.% of deionized water. The ratio of $Al(OH)_3$ to (85%) H_3PO_4 was 1:4.2 by weight, which corresponds to the molar ratio P/Al of about 3. The solution was slightly heated and mixed with a magnetic stirrer until it became clear. The 22M coating was sealed with orthophosphoric acid (85%) H_3PO_4. Basic sealing tests showed that impregnation of the (85%) H_3PO_4 sealant is more effective than the $Al(OH)_3$-(85%) H_3PO_4 solution in the case of the 22M coating. Compared to aluminum phosphate sealant, orthophosphoric acid is more reactive and has lower viscosity, so it penetrates into the dense coatings more easily. Porosity of the magnesia-stabilized coating in the as-sprayed state was lower than in the yttria-

Table 3 The Main Spray Parameters Used in the D-Gun Process

	HC Starck A706.072, A/S	HC Starck A727.054, A/S	HC Starck A840.1, F/C
Composition	Cr_2O_3	$8Y_2O_3$-ZrO_2	$65ZrO_2$-$35SiO_2$
Phase structure	α-Cr_2O_3	t′ + m-ZrO_2	t-$ZrSiO_4$
Particle size (μm)	−38 to +10	−45 to +10	−62 to +16
Acetylene flow rate (L/min)	22	22	22
Oxygen flow rate (L/min)	60	50	50
Air flow rate (L/min)	20	20	20
Spray distance (mm)	125	125	125

stabilized coating. This difference in porosity was probably a consequence of the dense and fine F/C feedstock powder. With both coatings the sealant was spread onto the surface just before the heat treatment. Heat treatment was performed at 300°C for 4 h in air.

2.4 Detonation Gun-Sprayed Dense Top Coatings.

The $8Y_2O_3$-ZrO_2, Cr_2O_3 and $ZrSiO_4$ layers were sprayed onto the thick 8Y coatings with detonation gun equipment (Perun-P, Paton Electric Welding Institute, Kiev, Ukraine) in order to get as dense a top coating as possible. Finer powder (compared to APS) was used in the detonation spray process because of the lower heating power. The thickness of the top layer was 70-400 μm. In this paper only the microstructural properties of detonation gun-sprayed top coats are compared with other sealed coatings. Spray parameters and powder information are listed in Table 3.

2.5 Characterization

The coating microstructure was determined by optical microscopy (OM, model Versamet 3, Union Co., Japan) and scanning electron microscopy (SEM) (model XL-30, Philips, Eindhoven, Netherlands). Energy dispersive spectrometry (EDS) (model DX-4, EDAX International, Mahwah, NJ) was used in elemental analysis in SEM studies. Polished microsections and fracture planes were prepared for microscopy studies. Coating phase structure was characterized by x-ray diffractometry (XRD), (Siemens D500, Karlsruhe, Germany) using Cu-Kα radiation (scan step 0.02°, step time 1.2 s). XRD analysis for the sealed coatings was made after grinding a 50 μm layer from the surface, because reaction products on the coating surface normally differ considerably from those below the surface. Coating microhardness ($HV_{0.3}$) profiles were determined by microhardness tester (Shimadzu, Kioto, Japan) from the coating cross section at 150-200 μm intervals. Results are presented as mean values of the three separate measurements at each depth.

2.6 Engine Tests

Engine tests were performed using a four-cylinder Valmet 411 DSJ high-speed (2400 rpm), diesel engine (Sisu Diesel Inc., Linnavuori, Finland). One cylinder of the test engine was modified for the data collection and coating testing. A specially designed piston head for thick coating was used in these tests (Fig. 1). Piston heads were plasma sprayed manually to the targeted TBC coating thickness of 1000 μm. Targeted bond coat thickness was 100 μm. As a result of the geometry of the piston head, some variation in coating thickness was observed.

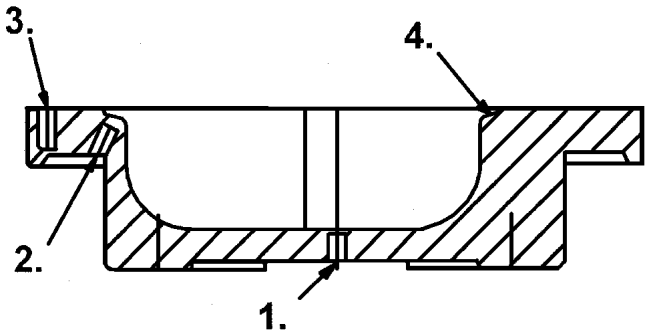

Fig. 1 Cross-sectional illustration of the piston head designed for the test engine: **(1-3)** sites for temperature probes (Templugs) and **(4)** machined chase for TTBC coating

Tests were carried out at the maximum load of the engine, because the aim was to increase the mean temperature of the combustion chamber as high as possible. The major objective of these engine tests was to examine the resistance of the phosphate-sealed TTBC against mechanical and thermal load. The duration of each test run was 3 h and coated piston heads were tested in separate runs. Measurements and calculations made from the data collected from the test runs showed that the mean surface temperature on the piston head was 560 °C and maximum pressure in the combustion chamber was 130 bar. The peak surface temperature during the engine cycle was estimated to be 300-400 °C higher than the mean temperature. Tested coatings were inspected visually and by microscopic studies of the microsections. The engine was also instrumented to study the engine's basic performance characteristics with coated and uncoated pistons. A finite element model (FEM) was used to simulate the surface temperatures of the coatings during the test. These basic engine performance results and FEM calculations will be published elsewhere.

2.7 Hot Corrosion Test

As-sprayed, phosphate-sealed, and laser-glazed coatings were exposed to $65Na_2SO_4$-$35V_2O_5$ (mol.%) deposit in air at 650 °C for 200 h. This composition was chosen to simulate the real deposits that build up in diesel engine combustion chamber walls in service. Mixed starting materials, Na_2SO_4 and V_2O_5, were melted in an alumina crucible at 800 °C for 2 h. The phase diagram of the Na_2SO_4-V_2O_5 system[24] is presented in Fig. 2. The solidified deposit was crushed manually after the heat treatment. The phase composition of the deposit after the melting was quite complex and XRD analysis showed traces of NaV_6O_{15}, NaV_3O_8, and Na_2SO_4. This composition, particularly the residual Na_2SO_4, indicates that homogenization of the starting materials was inadequate. The precipitation of the NaV_6O_{15} and NaV_3O_8 phases probably took place during the slow cooling of the deposit. NaV_6O_{15} was not presented in the Na_2SO_4-V_2O_5 system in Fig. 2, but the chemical composition of

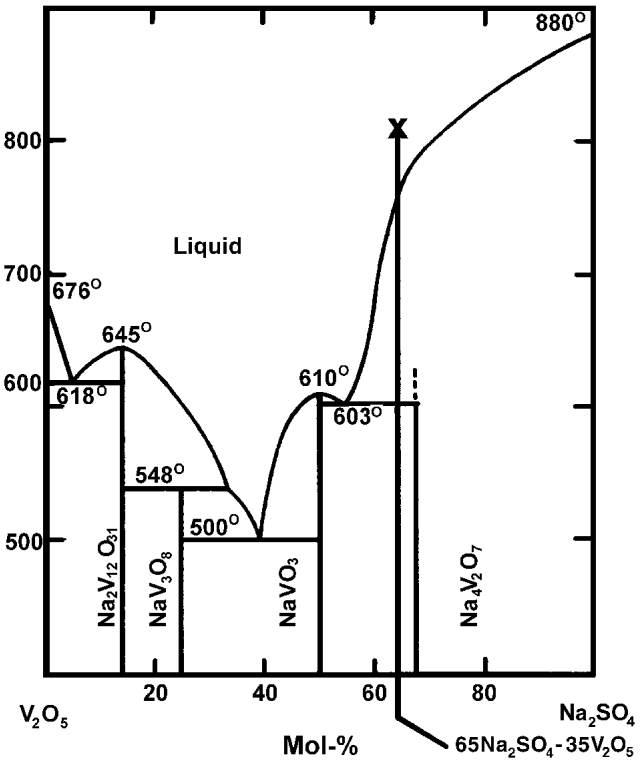

Fig. 2 Na_2SO_4-V_2O_5 phase diagram[24]

that phase is quite close to that of $Na_2V_{12}O_{31}$. Before the hot corrosion test, 10 mg of this solid deposit was placed on each specimen.

Specimens were inspected visually after the hot corrosion exposure and residues of the Na_2SO_4-V_2O_5 deposits were removed by light grinding. Microstructural changes of the coatings and reaction products caused by the deposit were determined by XRD. Tested coatings were also characterized by OM.

3. Results and Discussion

3.1 Coating Characterization

First, the sealing effect of different methods on coating microstructure was studied by examination of the coating cross sections with an optical microscope. Optical micrographs of 8Y, 8Y AP, and 8YL coatings are presented in Fig. 3(a-c). The thickness approximation for the sealed layer is presented with a dotted white line in each optical micrograph. Corresponding micrographs of the 22M coatings are presented in Fig. 4(a-c). As can be seen from Fig. 3(b) and 4(b), the phosphate-based sealants have penetrated into the coatings approximately 300-400 μm and decreased the coating porosity to some degree. In laser glazing, the melted zone in the both coatings was thinner, about 50-150 μm. Thicknesses of the detonation gun-sprayed D8Y, DCr_2O_3, and $DZrSiO_4$ top layers on 8Y coating were 70, 80, and 200 μm, respectively. For the detonation gun-sprayed coatings, the thickness was a function of the spray passes. The 8Y D8Y coating is presented in Fig. 5.

Microhardness profiles show the hardness increase in the sealed top layer of the coatings (Fig. 6). Hardness in the top layer of the laser-glazed coating was 1100-1250 $HV_{0.3}$, whereas in the phosphate sealed coating it was about 950 $HV_{0.3}$. Hardnesses of the D8Y, DCr_2O_3, and $DZrSiO_4$ coatings were 1010, 1180, and 800 $HV_{0.3}$, respectively. The microhardnesses of the as-sprayed coatings varied between 450 and 700 $HV_{0.3}$.

The laser-melted region was highly densified in 8YL and 22ML coatings, but some vertical cracks were detected, especially from the melted zone. Melting had occurred at a quite uniform layer in 8YL coating, but in magnesia-stabilized coating, the thickness of the melted layer varied by a fair amount. This difference probably results from the unequal laser beam absorption of these two coating materials. The 8YL coatings had a transparent and glass-like surface because of the better laser beam absorption and melting. In contrast, the surface of the 22ML coating was quite rough and inhomogeneous. It seemed that the surface of the 22ML coating had melted only locally. The color of the yttria-stabilized zirconia coatings changed from light gray to transparent yellow because of the laser-glazing process. The white color of the 22M did not change in the laser treatment. Close-up photographs and SEM top-view images of the glazed TTBC coatings are presented in Fig. 7.

SEM studies showed the columnar/dendritic structure of the laser-glazed zone. The structure of the 8YL coating is presented in Fig. 8. From the fracture surface of the coating, some voids could be detected at the lower region of the melted zone. Voids are marked with white arrows in Fig. 8. Columnar structure of the 22ML coating was not possible to detect from the fracture surface specimen, but backscattered electron images taken from the polished microsection showed the columnar/dendritic nature of the properly glazed zone (Fig. 9). Some small sized pores could be found from the glazed zone, but the pore size distribution was smaller if compared to 8YL coating.

The microstructural change in the phosphate-sealed coatings can be clearly seen in optical micrographs in Fig. 3(b) and 4(b). The sealed zone is denser in 22M OPA coating if compared to the 8Y AP coating, but also the porosity of the magnesia-stabilized coating was lower in the as-sprayed state. Phosphate phases were difficult to observe in SEM/EDS studies, but our earlier study,[23] showed the presence of the aluminum-rich bonding phase in the 8Y AP coating structure. The bonding effect of the sealant can be seen in the SEM micrograph shown in Fig. 10, taken from the fracture surface of the sealed top layer of the 8Y AP coating. Typically, the fracture surface of the zirconia coating is coarse, and lamellar structure and individual lamellae are easily detected. In the denser regions of the phosphate-sealed coating, marked with arrows, the fracture surface is quite plain and just some of the splat boundaries could be detected.

XRD phase diagrams for the coating surfaces of the yttria-stabilized zirconia coatings are presented in Fig. 11(a-d). The $8Y_2O_3$-ZrO_2 spray powder (A/S) consists of tetragonal (t-ZrO_2), cubic (c-ZrO_2), and monoclinic (m-ZrO_2) zirconia. In the as-sprayed coating, the metastable t′-ZrO_2 was the major phase, but some minor traces of the c-ZrO_2 and m-ZrO_2 still appeared. In the 8Y AP coating the amount of m-ZrO_2 was slightly increased compared to the as-sprayed coating. Any reaction products caused by phosphate-sealing treatment could not be found by XRD. This may be the consequence of the low concentration of the bonding phases or their amorphous microstructure. In the laser-glazed coating, the phase structure was purely t′-ZrO_2. The

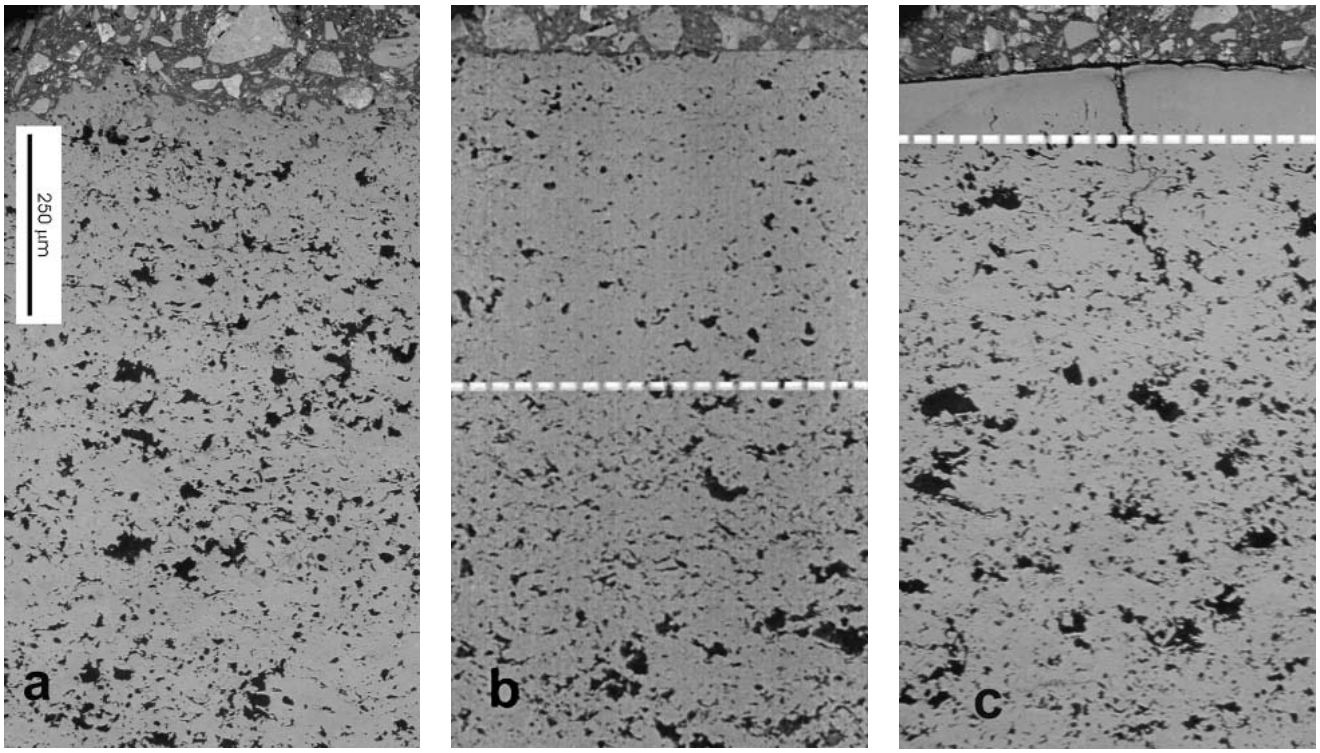

Fig. 3 Optical micrographs of the $8Y_2O_3$-ZrO_2 coatings: **(a)** 8Y, **(b)** 8Y AP, and **(c)** 8YL

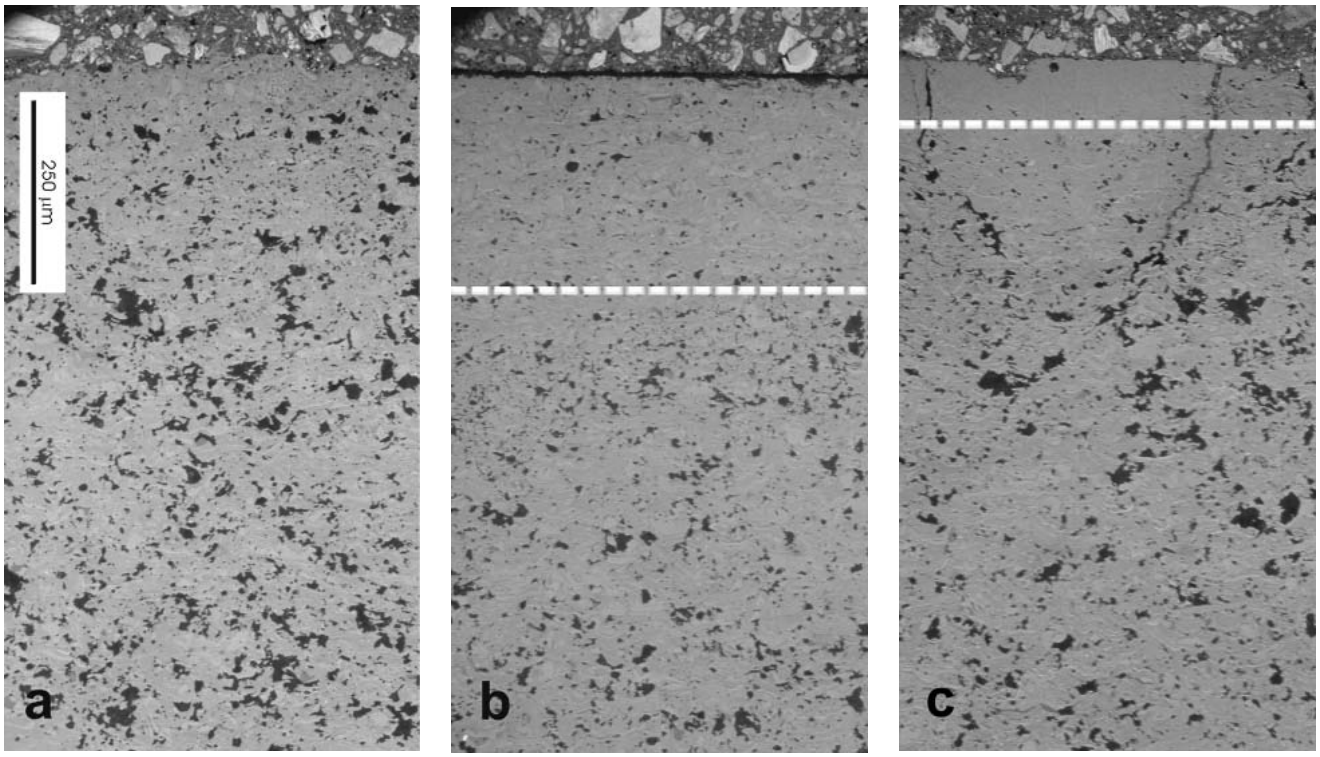

Fig. 4 Optical micrographs of the 22MgO-ZrO_2 coatings: **(a)** 22M, **(b)** 22M OPA, and **(c)** 22ML coating

relative intensity of the individual diffraction peaks was changed greatly; this is due to the columnar grain orientation, caused by laser-glazing process. Detailed XRD studies from the 2θ-region of 72-76° showed that the lattice parameters of the glazed coating differ in some degree if compared to as-sprayed coating (Fig. 12). There is a wider gap between the peaks t′ (400) and t′ (004)

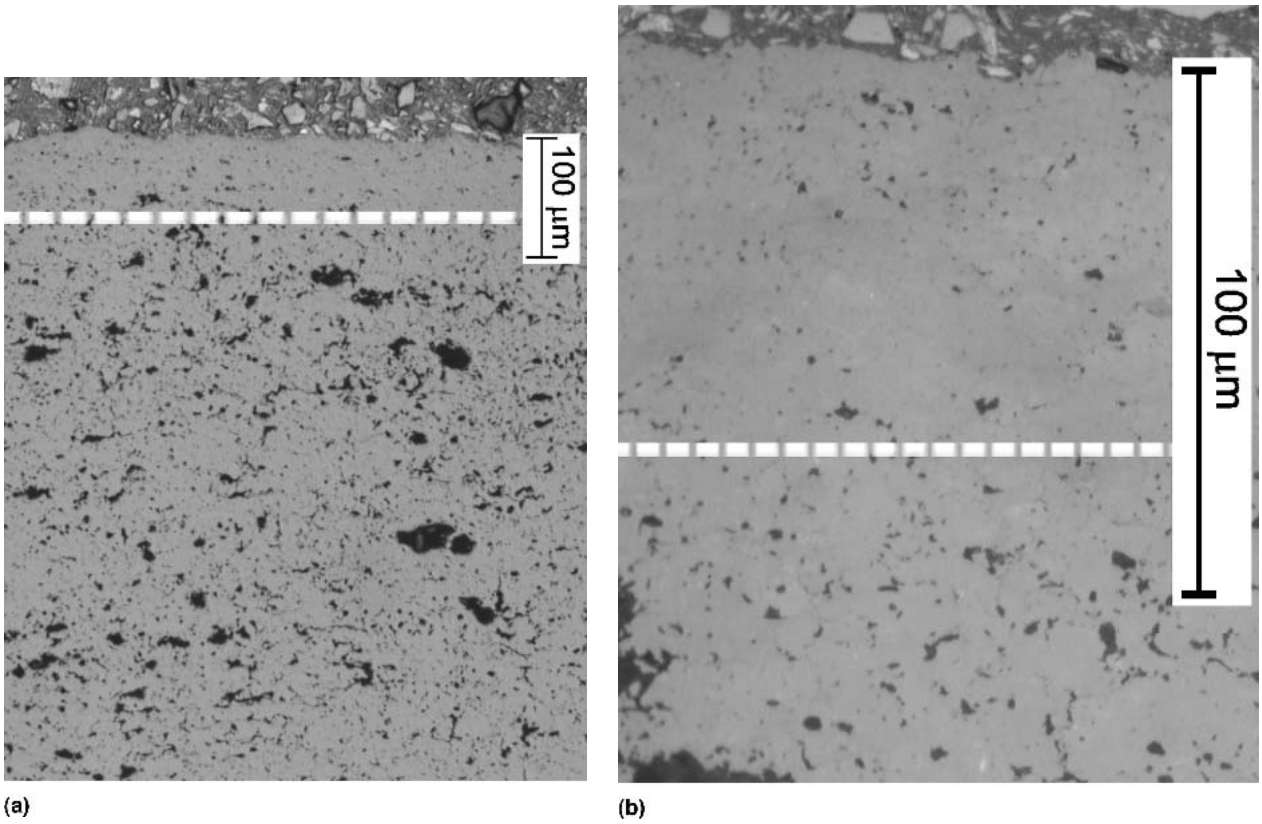

Fig. 5 Optical micrographs of the 8Y D8Y coating

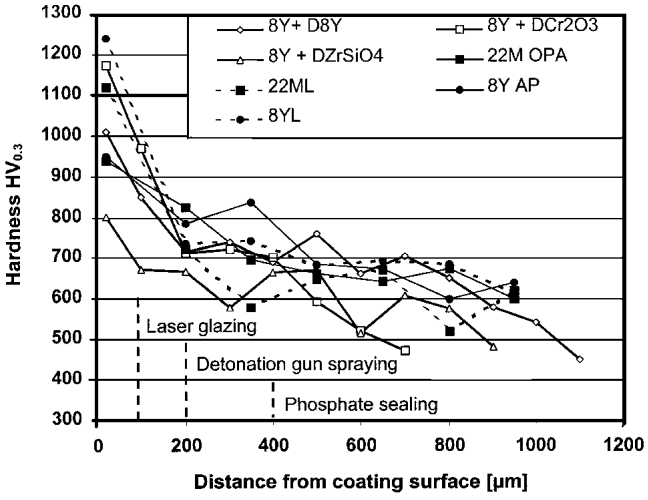

Fig. 6 Microhardness profiles for sealed coatings

in the laser-glazed coating. This is an indication of the slightly lower concentration of the Y_2O_3 in ZrO_2 structure.[25] Yttria may have locally redistributed in zirconia structure during solidification after the glazing process.

XRD data for the surface of the magnesia-stabilized zirconia coatings are presented in Fig. 13(a-d). The phase structure of the 22MgO-ZrO_2 spray powder (F/C) was mainly cubic (c-ZrO_2) with some free cubic MgO phase (c-MgO, periclase). These same phases were present in the as-sprayed coating, but quite intense broadening of the c-ZrO_2 peaks could be detected. Peak broadening of the c-ZrO_2 in the as-sprayed 22M coating may be a consequence of the concentration variations of MgO in the c-ZrO_2 structure. Phosphate-based sealing affected just slightly the phase structure of the 22M coating when measured after the 50 µm top layer was ground off. Some traces of the reaction products still caused by the sealant could be detected from the 2θ-region at 15-30°. Intensity of these peaks and the peak/background ratio was too low to use them in identification. If just the surface roughness of the 22M OPA coating was smoothed instead of grinding away 50 µm, clear zirconium phosphate (ZrP_2O_7) peaks were identified. It seemed to be the most probable crystalline reaction product between the 22M coating and orthophosphoric acid.

In the 22ML coating, in addition to the c-ZrO_2 structure, some rhombohedral $Mg_2Zr_5O_{12}$ could be detected. EDS analysis showed that in the lighter region of the melted zone, the concentration of the MgO was ~8 wt.%, and in darker region, the concentration was ~17 wt.%. These regions are marked with arrows in Fig. 9. The vapor pressure of MgO, in the molten state during the laser glazing, is much higher than that of ZrO_2. The decrease of total amount of MgO in the coating structure is a consequence of its vaporization during the laser-glazing process. Peak broadening of the c-ZrO_2 phase in the 22ML coating did not occur as it did in the as-sprayed coating. This is probably a consequence of the uniform redistribution and lower concen-

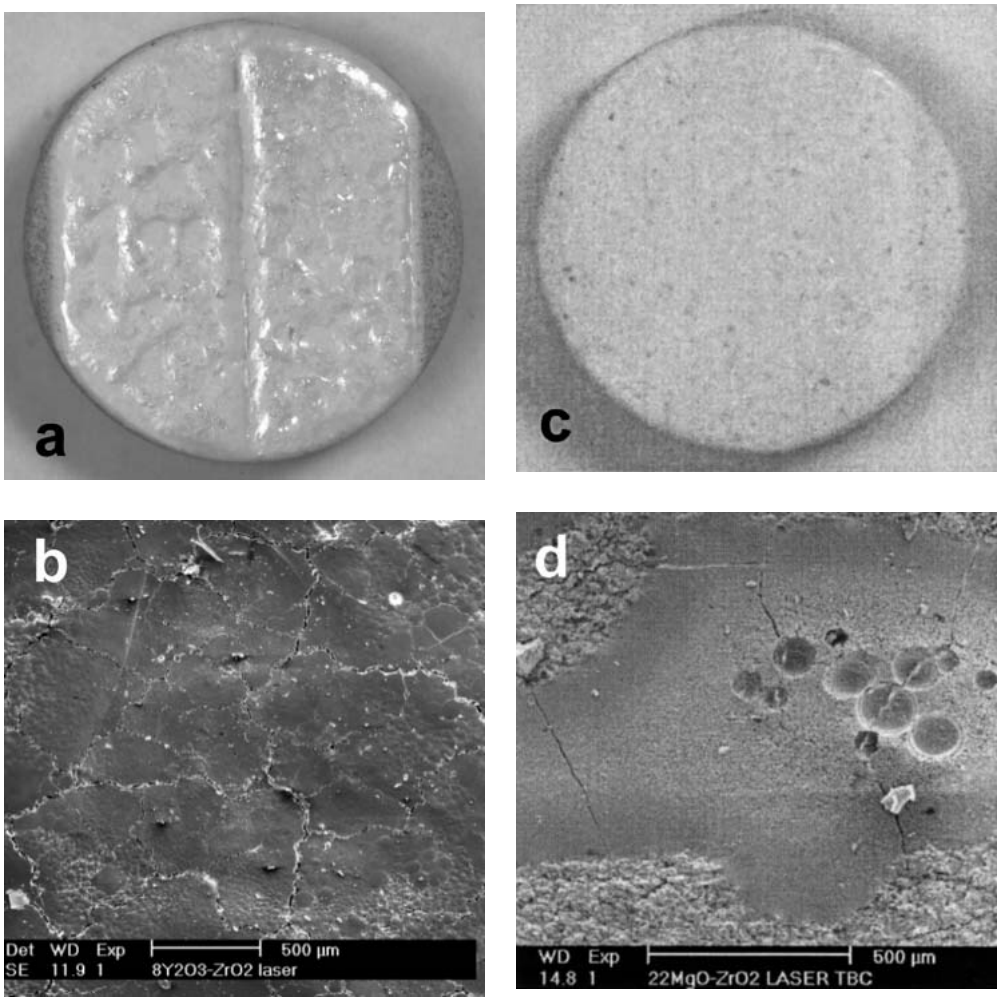

Fig. 7 Top view of the laser-glazed coatings: **(a)** close-up photograph of the 8YL coating, **(b)** SEM micrograph of the 8YL coating, **(c)** close-up photograph of the 22ML coating, and **(d)** SEM micrograph of the 22ML coating

tration of the magnesia in the c-ZrO_2 structure after the glazing process.

Detonation gun-sprayed D8Y, DCr_2O_3, and D$ZrSiO_4$ coatings showed considerably lower porosities compared to APS-sprayed 8Y coating. The dense and crack-free structure of the detonation gun-sprayed coatings indicated sufficient melting of ceramic powders. The 8Y_2O_3-ZrO_2 feedstock powder (A727.054) contained a minor fraction of m-ZrO_2. XRD studies showed that the phase structure of the D8Y coating was t′-ZrO_2. This was also an indication of the proper melting of the 8Y_2O_3-ZrO_2 powder. Cr_2O_3 powder and the DCr_2O_3 coating consisted mostly of the eskolaite type hexagonal α-Cr_2O_3. Some minor amounts of Cr, CrO, and Cr_3O_4 were also detected from the sprayed coating. These minor phases are probably a consequence of the decomposition of the hexagonal α-Cr_2O_3 structure during spraying. D$ZrSiO_4$ coating consisted mostly of the t′-ZrO_2 and m-ZrO_2 phases. This indicates that $ZrSiO_4$ structure has decomposed during spraying and some amount of SiO_2 has formed a solid solution with ZrO_2 and stabilized the t′-ZrO_2 structure. The rest of the SiO_2 has obviously formed an amorphous structure during rapid cooling in the spray process.

3.2 Engine Tests

Visual examination of the coated piston crowns showed some vertical cracks in phosphate-sealed coatings, but no coating spallation was observed. In the 22M OPA coating the crack density was higher as compared to the 8Y AP coating. Damage in unsealed coatings was not detected visually. Cross-sectional specimens were cut from the rim region of the piston bowl. Temperature measurements and FEM calculations showed that the surface temperature was highest in this region. Micrographs of the engine-tested coatings are presented in Fig. 14. During microsectional examination, some cracks that were parallel to the piston surface were found in the 22M OPA coating. Only a few vertical cracks were detected in the 8Y AP coating. Unsealed coatings did not show any microstructural changes.

Cracking of the sealed coatings can be explained by the denser structure of the outer layer of the coating. The capability of coating surface to adapt to thermal cycling loading had obviously decreased, because of the lower porosity and lower microcrack density of the sealed coating. Because the sealed coatings did not spall during the test runs, it is difficult to estimate their service life. The effect of vertical cracks induced by the engine

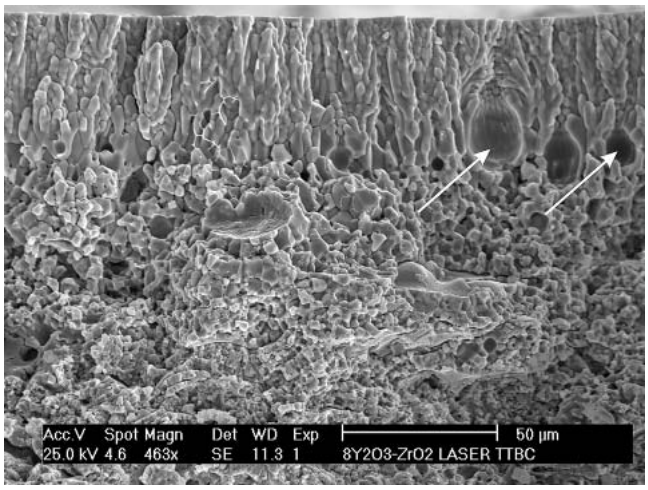

Fig. 8 Fracture surface of the 8YL coating

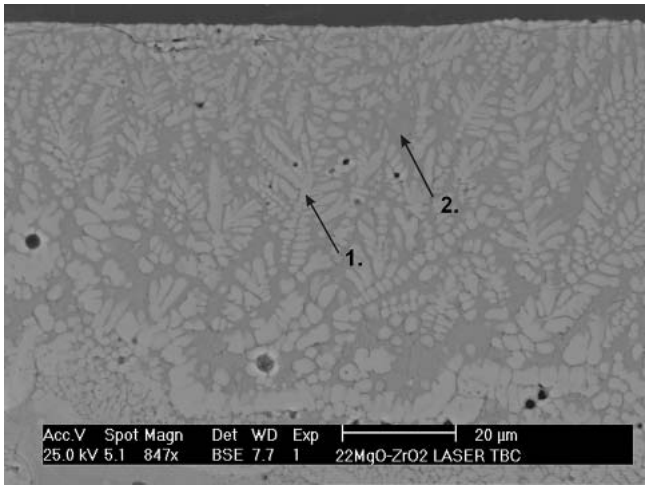

Fig. 9 SEM backscattered electron image of the polished cross section of the 22ML coating

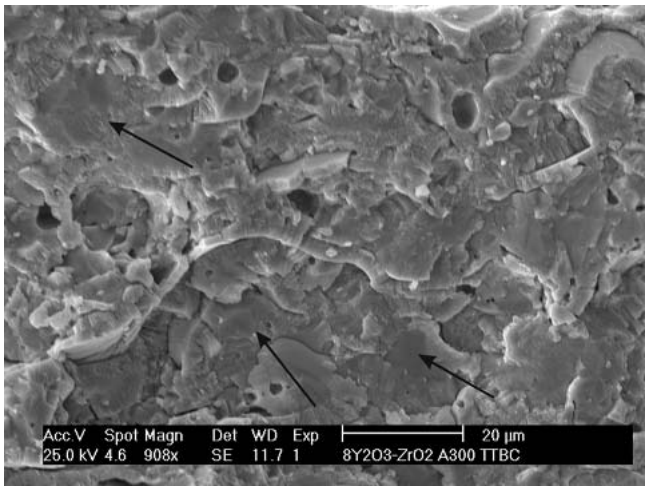

Fig. 10 Fracture surface of the 8Y AP coating

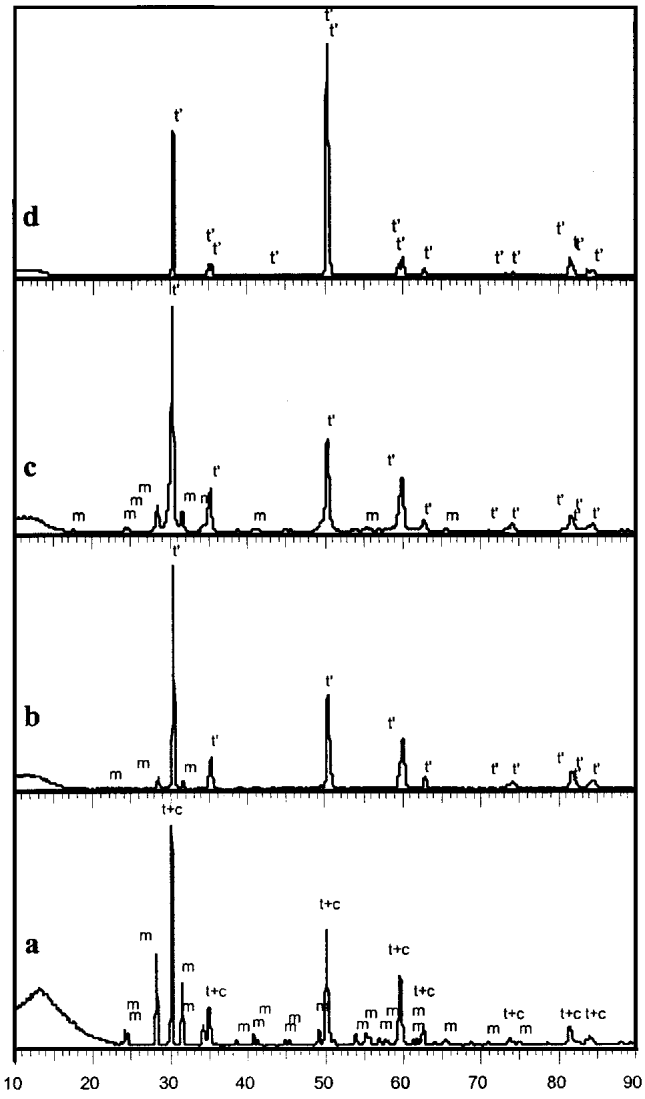

Fig. 11 XRD diagrams for $8Y_2O_3$-ZrO_2 powder and coating surfaces: m = m-ZrO_2, t′ = t′-ZrO_2, t = t-ZrO_2, c = c-ZrO_2. **(a)** Spray powder, **(b)** 8Y coating, **(c)** 8Y AP coating, and **(d)** 8YL coating.

test could be positive in long-term engine runs when thermal cycling resistance is considered. In that case, the other beneficial properties of the sealed coatings, such as better erosion and hot corrosion resistance, could be utilized.

3.3 Hot Corrosion Test

First, the visual inspection of the exposed specimens showed that the 22M coatings were in better condition than were the 8Y coatings. All coatings showed color changes to different shades of brown, yellow, and green. The 8Y and 8Y AP coatings fractured and spalled during the post-test cooling. Cracking was very violent and coating fragments bounced off the substrate. Coating phase changes and reactions with the molten deposit, as well as solidification of the deposit into the coating defects during cooling, probably had caused strong internal stresses within the coating. The 22M OPA coating also exhibited stress-induced spalling, but the coating remained in one piece. The 22M coating

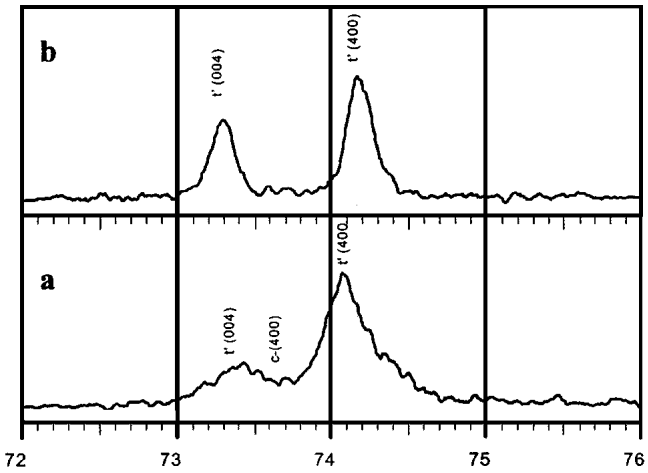

Fig. 12 XRD diagrams of the $8Y_2O_3$-ZrO_2 coating surfaces from the 2θ-region 72 to 76°: **(a)** 8Y coating and **(b)** 8YL coating

and both laser-glazed coatings did not spall during or after the test. Cross-sectional SEM images of the 8YL coating, after the hot corrosion test, are presented in Fig. 15. A vanadium-rich deposit was found by EDS analysis from the crack tip 150 μm below the surface and it is marked with an arrow. This means that molten corrodant can penetrate under the sealed surface layer through the typical vertical cracks in laser-glazed coatings.

XRD studies showed the phase changes in zirconia and the reaction products with the coating and the Na_2SO_4-V_2O_5 deposit. The studies also revealed the composition of the white-colored residue deposit on the coatings surface. It consisted mostly of Na_2SO_4 and it had obviously solidified during the exposure. The most common phenomenon with all coatings was the increase of the proportion of the m-ZrO_2. In the laser-glazed coatings, the amount of m-ZrO_2 was much lower than in the other coatings. Zirconia destabilization (phase changes t′-ZrO2 → c-ZrO_2, t-ZrO_2, and c-ZrO_2, t-ZrO_2 → m-ZrO_2) had occurred because of the reactions between the stabilizing oxides Y_2O_3, MgO, and the Na_2SO_4-V_2O_5 deposit.

XRD diagrams of the 8Y, 8Y AP, and 8YL coatings are presented in Fig. 16(a-c). In all cases Y_2O_3 had reacted with vanadium and formed YVO_4. This reaction (Eq 1) was reported in several studies[26-28] and it is known to be a problem with yttria-stabilized zirconia in vanadium-containing environments at a temperature range of 600-900 °C.

$$Y_2O_3 \text{ (in t′-}ZrO_2\text{)} + V_2O_5 \leftrightarrow 2YVO_4 \text{ with formation of m-}ZrO_2 \quad \text{(Eq 1)}$$

XRD showed some free Na_2SO_4 for the laser-glazed coating. It probably exists in the groove between two laser-glazing tracks and could not be removed by light grinding. The major phase in the reference and 8Y AP coating was m-ZrO_2, whereas the t′-ZrO_2 dominated the structure of the laser-glazed coating. There are two possible reasons for this: (1) either the transformed t′-ZrO_2 structure in laser-glazed coating was more resistant to reaction with the deposit, or (2) the specific surface area for the corrosion reaction was much lower, because of the very dense glazed layer.

XRD diagrams of the exposed 22M, 22M OPA, and 22ML specimens are presented in Fig. 17(a-c). Destabilization of the c-ZrO_2 took place in all coatings. Again, the laser-glazed coating was the best performing coating in this test. In the laser-glazed coating, the rhombohedral $Mg_2Zr_5O_{12}$ appeared to be a more stable phase in the test environment compared to c-ZrO_2. Some unidentified diffraction peaks were present in the XRD diagram for 22M OPA and 22ML coatings. These peaks did not fit exactly to any reaction products expected, but some correlations were found with MgV_2O_6. Other expected reaction products according to the phase diagram of MgO and V_2O_5[29] were $Mg_2V_2O_7$, MgV_6O_{17}, and $Mg_3V_2O_8$, but these phases were not found from exposed 22M coatings. MgO has been reported to form $MgSO_4$ in the presence of Na_2SO_4(l) and SO_3(g).[30] Magnesium sulfate was not found in XRD studies. In as-sprayed coatings there was some free c-MgO phase, which completely disappeared from all coatings during the exposure, according to XRD studies. Lack of the free c-MgO and destabilization of the c-ZrO_2 in exposed coatings mean that MgO reacted to some extent with the Na_2SO_4-V_2O_5 deposit.

4. Conclusions

Three different sealing procedures of the thick thermal barrier coating were described: (1) impregnation of phosphate-based sealant, (2) surface melting by laser glazing, and (3) spraying of dense top coating with detonation gun. Coating microstructural properties were characterized and some thermal and mechanical properties were studied. The most important results are listed below.

- In laser-glazed TTBCs, the thickness of the melted zone was 50-150 μm. With phosphate-based sealing treatments it was possible to apply 300-400 μm thick densified top layers. Detonation gun-sprayed top layers were 70-200 μm thick.
- Microhardness of the outermost portion in the sealed top layer in laser-glazed coatings was 1100-1250 $HV_{0.3}$ and ~950 $HV_{0.3}$ in phosphate-sealed coatings. Microhardnesses of the detonation gun-sprayed coatings varied between 800 and 1180 $HV_{0.3}$. The microhardnesses of the as-sprayed coatings varied between 450 and 700 $HV_{0.3}$.
- Phase structure of the as-sprayed 8Y coating changed in laser glazing from t′-ZrO_2, c-ZrO_2, and m-ZrO_2 to t′-ZrO_2. Lattice parameters of the t′-ZrO_2 in the laser-glazed coatings were changed by reduced Y_2O_3 content in the coating. Phosphate phases were not possible to detect by XRD from the 8Y AP coating.
- In the laser-glazing process, the phase structure of the magnesia-stabilized zirconia changed from c-ZrO_2 to a mixture of rhombohedral $Mg_2Zr_5O_{12}$ and c-ZrO_2. Unidentified diffraction peaks were detected in XRD studies of the 22M OPA coating. These peaks might belong to the phosphate-based bonding phase.
- Detonation gun spraying could be used to produce denser ceramic top layers onto conventionally sprayed TTBCs.
- The 8Y and 22M coatings passed the engine test without any damage. In phosphate-sealed coatings, some vertical microcracks were built up during the test run. However, no spallation was observed in any case.

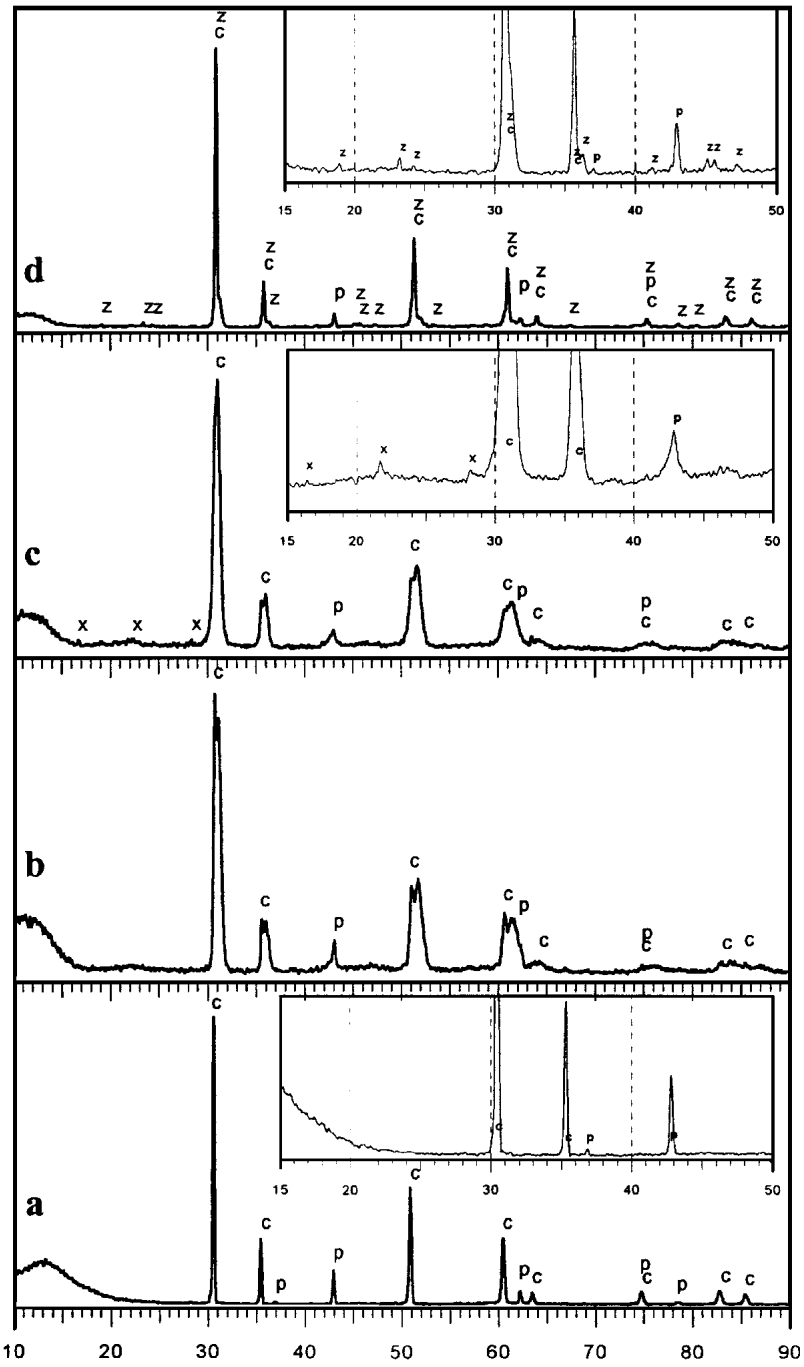

Fig. 13 XRD diagrams for 22MgO-ZrO_2 powder and coating surfaces: c = c-ZrO_2, p = c-MgO (periclase), x = unidentified phosphate phase, z = $Mg_2Zr_5O_{12}$. **(a)** Spray powder, **(b)** 22M coating, **(c)** 22M OPA coating, and **(d)** 22ML coating

- Critical phase changes and corrosion reactions were observed in 8Y, 8Y AP, and 8YL coatings after the hot corrosion test. The amount of the m-ZrO_2 increased greatly and YVO_4 formed in all cases. The laser-glazed coating performed best in the hot corrosion test.
- The 22M, 22M OPA, and 22ML coatings were slightly more resistant to Na_2SO_4-V_2O_5 than were yttria-stabilized coatings, if coating color changes and cracking are considered. Coatings also suffered undesired zirconia phase changes, but in laser-glazed coatings, the $Mg_2Zr_5O_{12}$ phase seemed to be more resistant against hot corrosion than did c-ZrO_2.

Acknowledgments

Results in this paper were collected from studies carried out during the year 2000. The work was financed by Finnish indus-

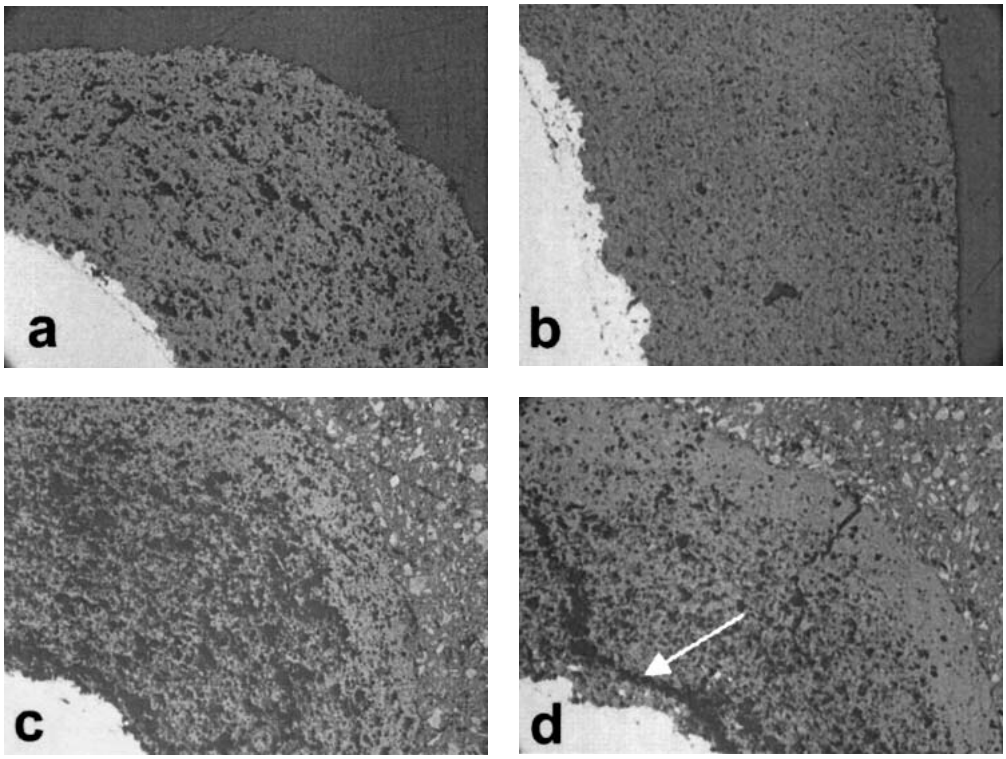

Fig. 14 Optical micrographs of the engine tested coatings: **(a)** 8Y coating, **(b)** 22M coating, **(c)** 8Y AP coating, and **(d)** 22M OPA coating

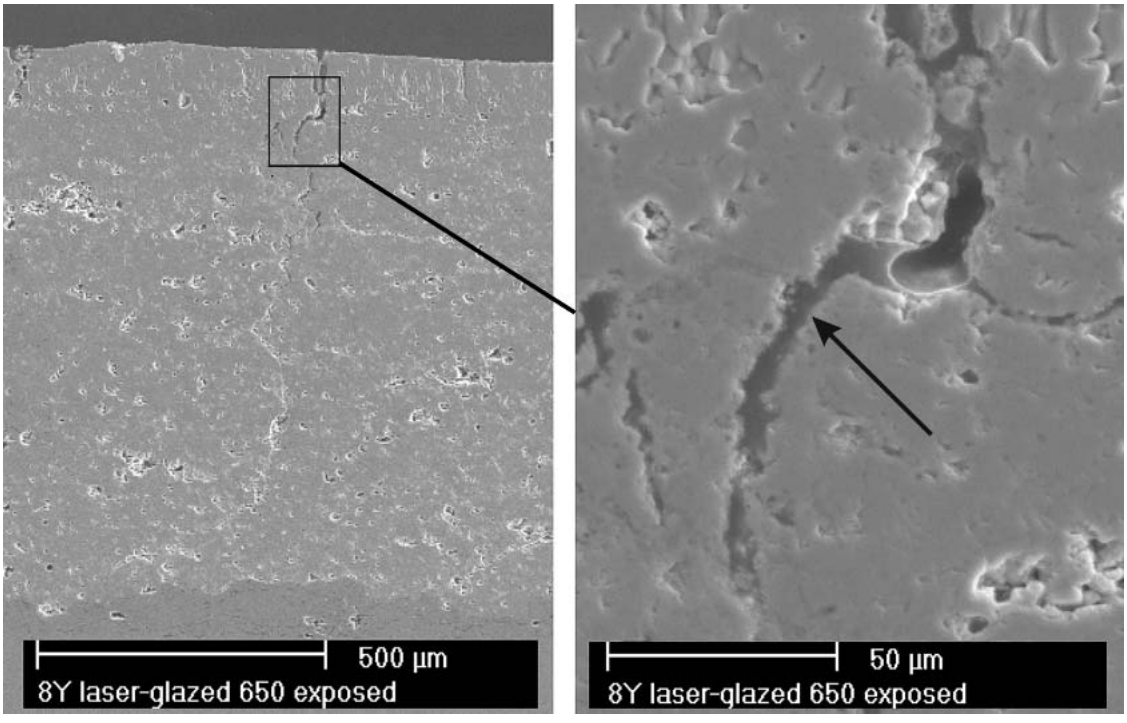

Fig. 15 SEM micrograph of the hot corrosion tested 8YL coating

try, TEKES, and The Academy of Finland. The authors are grateful to financial supporters, and to Ms. Sari Iltanen and Mr. Mikko Kylmälahti for assistance in experimental work. The authors also thank the Helsinki University of Technology/Institute of Internal Combustion Engine Laboratory for performing the engine tests.

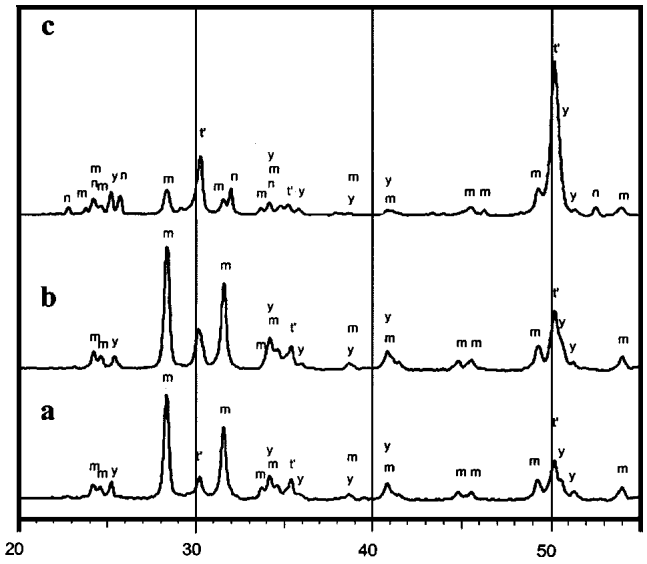

Fig. 16 XRD diagrams for hot corrosion tested $8Y_2O_3$-ZrO_2 coatings: m = m-ZrO_2, t′ = t′-ZrO_2, y = YVO_4, n = Na_2SO_4. **(a)** 8Y coating, **(b)** 8Y AP coating, and **(c)** 8YL coating

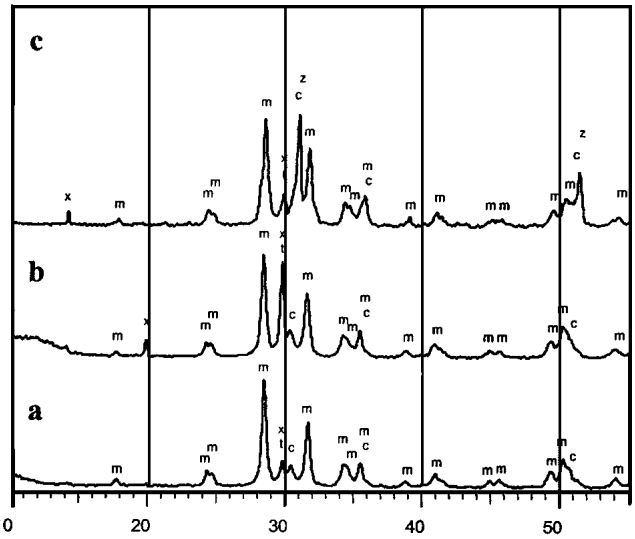

Fig. 17 XRD diagrams for hot corrosion tested 22MgO-ZrO_2 coatings: m = m-ZrO_2, c = c-ZrO_2, z = $Mg_2Zr_5O_{12}$, t = t-ZrO_2, x = unidentified peak. **(a)** 22M coating, **(b)** 22M OPA coating, and **(c)** 22ML coating

References

1. D.N. Assanis: "Thin Thermal Barrier Coatings for Internal Combustion Engine Components," *Int. J. Mater. Prod. Technol.*, 1989, *4*(3), pp. 232-43.
2. I. Kvernes: "Potential of Coatings in Diesel Engines" in *Proceedings of the Conference: High Temperature Materials for Power Engineering 1990*, Kluwer Academic Publishers, Dordrecht, The Netherlands, 1990, pp. 843-64.
3. T.M. Yonushonis: "Overview of Thermal Barrier Coatings in Diesel Engines," *J. Thermal Spray Technol.*, 1997, *6*(1), pp. 50-56.
4. M.B. Beardsley: "Thick Thermal Barrier Coatings for Diesel Engines," *J. Thermal Spray Technol.*, 1997, *6*(2), pp. 181-86.
5. A. Ohmori, Z. Zhou, K. Inoue, K. Murakami, and T. Sasaki: "Sealing and Strengthening of Plasma-Sprayed ZrO_2 Coating by Liquid Mn Alloy Penetration Treatment" in *Thermal Spraying: Current Status and Future Trends*, A. Ohmori, ed., High Temperature Society of Japan, Osaka University, Osaka, Japan, 1995, pp. 549-54.
6. H.L. Tsai and P.C. Tsai, "Performance of Laser-Glazed Plasma-Sprayed (ZrO_2-12wt.%Y_2O_3)/(Ni-22wt.%Cr-10wt.%Al-1wt.%Y) Thermal Barrier Coatings in Cyclic Oxidation Tests," *Surf. Coat. Technol.*, 1995, *71*, pp. 53-59.
7. H. Kuribayashi, K. Suganuma, Y. Miyamoto, and M. Koizumi: "Effect of HIP Treatment on Plasma-Sprayed Ceramic Coating Onto Stainless Steel," *Am. Ceram. Soc. Bull.*, 1986, *65*(9), pp. 1306-10.
8. G. John and T. Troczynski: "Surface Modification of Thermal Sprayed Coatings" in *Thermal Spray: Practical Solutions for Engineering Problems*, C.C. Berndt, ed., ASM International, Materials Park, OH, 1996, pp. 483-88.
9. K. Moriya, W. Zhao, and A. Ohmori: "Improvement of Plasma-Sprayed Ceramic Coatings Treated by Sol-Gel Process" in *Thermal Spraying: Current Status and Future Trends*, A. Ohmori, ed., High Temperature Society of Japan, Osaka University, Osaka, Japan, 1995, pp. 1017-21.
10. R. Rajendran, V.S. Raja, R. Sivakumar, and R.S. Srinivasa, "Reduction of Interconnected Porosity in Zirconia-Based Thermal Barrier Coating," *Surf. Coat. Technol*., 1995, *73*, pp. 198-200.
11. T. Troczynski, Q. Yang, and G. John: "Post-Deposition Treatment of Zirconia Thermal Barrier Coatings Using Sol-Gel Alumina," *J. Thermal Spray Technol.*, 1999, *8*(2), pp. 229-34.
12. J. Knuuttila, P. Sorsa, and T. Mäntylä: "Sealing of Thermal Spray Coatings by Impregnation," *J. Thermal Spray Technol.*, 1999, *8*(2), pp. 249-57.
13. R.L. Jones: "Some Aspects of the Hot Corrosion of Thermal Barrier Coatings," NASA Conference Publication 3312, Thermal Barrier Workshop, Cleveland, OH, 1995, pp. 217-33.
14. A.J. Scharman and T.M. Yonushonis: "Ceramic Thermal Barrier Coating for Rapid Thermal Cycling Applications," United States Patent no. 5,320,909, June 14, 1994.
15. D.W. Parker: "Thermal Barrier Coatings for Gas Turbines, Automotive Engines and Diesel Engines," *Mater. Design*, 1992, *13*(6), pp. 345-51.
16. M.F. Winkler and D.W. Parker: "Thermal Barrier Coatings for Diesel Engines—Ten Years of Experience," SAE Technical Paper Series, No. 922438, SAE, Warrendale, PA, 1992.
17. K. Osawa, R. Kamo, and E. Valdmanis: "Performance of Thin Thermal Barrier Coating on Small Aluminum Block Diesel Engine," SAE Technical Paper Series, No. 910461, Warrendale, PA, 1991.
18. M. Vittal, J.A. Borek, D.A. Marks, A.L. Boehman, D.A. Okrent, and A.P. Bentz: "The Effects of Thermal Barrier Coatings on Diesel Engine Emissions," *Transactions of the ASME*, 1999, *121*, pp. 218-25.
19. E. Kumpulainen, M. Vippola, P. Vuoristo, P. Sorsa, and T. Mäntylä: "Characteristics of Phosphoric Acid Sealed Ceramic Oxide Coatings" in *Thermal Spray: Practical Solutions for Engineering Problems*, C.C. Berndt, ed., ASM International, Materials Park, OH, 1996, pp. 489-91.
20. K. Niemi, P. Sorsa, P. Vuoristo, and T. Mäntylä: "Thermally Sprayed Alumina Coatings with Strongly Improved Wear and Corrosion Resistance" in *Thermal Spray Industrial Applications*, C.C. Berndt and S. Sampath, ed., ASM International, Materials Park, OH, 1994, pp. 533-36.
21. E. Leivo, M. Vippola, P. Sorsa, P. Vuoristo, and T. Mäntylä: "Wear and Corrosion Properties of Plasma Sprayed Al_2O_3 and Cr_2O_3 Coatings Sealed by Aluminum Phosphates," *J. Thermal Spray Technol.*, 1997, *6*(2), pp. 205-10.
22. J. Knuuttila, S. Ahmaniemi, and T. Mäntylä: "Wet Abrasion and Slurry Erosion Resistance of Sealed Oxide Coatings" in *Thermal Spray: Meeting the Challenges of the 21st Century*, C. Coddet, ed., ASM International, Materials Park, OH, 1998, pp. 145-50.
23. S. Ahmaniemi, P. Vuoristo, and T. Mäntylä: "Effect of Aluminum Phosphate Sealing Treatment on Properties of Thick Thermal Barrier Coat-

ing" in *Thermal Spray: Surface Engineering via Applied Research*, C.C. Berndt, ed., ASM International, Materials Park, OH, 2000, pp. 1081-86.
24. R.S. Roth, T. Negas, and L.P. Cook: *Phase Diagrams for Ceramists*, Vol. IV, Fig. 5127, The American Ceramic Society, Columbus, OH, 1981, p. 89.
25. R. Taylor, J.R. Brandon, and P. Morrell: Microstructure, "Composition, and Property Relationships of Plasma-Sprayed Thermal Barrier Coatings," *Surf. Coat. Technol.*, 1992, *50*, pp. 141-49.
26. R.L. Jones: "The Development of Hot-Corrosion-Resistant Zirconia Thermal Barrier Coatings," *Mater. High Temp.*, 1991, *9*(4), pp. 228-36.
27. D.W. Susnitzky, W. Hertl, and C.B. Carter: "Vanadia-Induced Transformations in Yttria-Stabilized Zirconia," *Ultramicroscopy*, 1989, *30*, pp. 233-41.
28. B.R. Marple, J. Voyer, C. Moreau, and D.R. Nagy: "Corrosion of Thermal Barrier Coatings by Vanadium and Sulfur Compounds," *Mater. High Temp.*, 2000, *17*(3), pp. 397-412.
29. R.S. Roth, T. Negas, and L.P. Cook: *Phase Diagrams for Ceramists*, Vol. IV, Fig. 5163, The American Ceramic Society, Columbus, OH, p. 104.
30. R.L. Jones: "Thermogravimetric Study of the 800°C Reaction of Zirconia Stabilizing Oxides with SO_3-$NaVO_3$," *J. Electrochem. Soc.*, 1992, *139*(10), pp. 2794-99.